SIMULATION OF FLOW AROUND A CIRCULAR CYLINDER FITTED WITH STRAKES

Rafael S. Gioria, rafaelgioria@yahoo.com.br
Ivan Korkischko, ivan.korkischko@poli.usp.br
Julio Romano Meneghini, jmeneg@usp.br
NDF, Dept. Mech. Eng., Escola Politécnica of University of São Paulo, Brazil

Abstract. *We investigate the mechanism of suppression of vortex-induced vibration by using helical strakes. Computational simulation of the flow around a fixed circular cylinder fitted with strakes are performed in order to ratify that the main aspect on the suppression is the decrease in the vortex shedding correlation along the span. To support the latter allegation, we employ a spatial correlation of the velocity fields. We also observe that the vortex wake is formed farther downstream and we can identify this as a secondary mechanism of vortex-induced vibrations suppression. A comparison of velocity fields from particle image velocimetry with the simulation results is presented in order to support the simulation analysis. We also present the resulting fluid forces on the body in comparison to experimental measurements.*

Keywords: *Vortex-Induced Vibration, Helical Strakes, Cylinder Wake*

1. INTRODUCTION

Vortex-induced vibrations (VIV) are challenging phenomena in theoretical studies and applied engineering. Some reviews on vortex-induced vibrations have been published, for example Bearman (1984) and Williamson and Govardhan (2004), and many of them are focused on circular cylinder vibration.

Several methods of VIV suppression have been proposed and reviewed as an effort to minimize the consequences of these vibrations. One of the main consequence of VIV is the fatigue stress on the structure. Two extensive revisions on VIV suppressors are Zdravkovich (1981) and Choi *et al.* (2008). Some of the most common VIV suppressors are the helical strakes due to its geometrical simplicity, its effectiveness and the possibility of installation on offshore structures. Herein we deal with helical strakes with three-start configuration. The main geometrical aspects of strakes are its height h and its pitch p.

Many works investigated the effectiveness of the strakes as VIV suppressors. Korkischko and Meneghini (2010) show that the effectiveness of the strakes is more associated to its height than to its pitch in water flow around a single circular cylinder fitted with strakes. Although the strakes effectiveness has been assessed, the suppression mechanism is yet not well established. Most works point out that the main aspect on the suppression is the decrease in the vortex shedding correlation along the span. Some others also attribute the vortex-induced vibrations suppression to the formation of vortices around a straked cylinder farther downstream than on the flow around a bare one.

In such case, computational simulations are appropriate to asses the details of flow dynamics in ways that is not feasible in experiments. Nevertheless, experimental observations are still the paradigm of the simulations presented herein. The flow around a circular cylinder fitted with strakes has not been widely simulated. Constantinides and Oakley (2006) presented, to the authors knowledge, the only work with numerical simulations of flow around a cylinder fitted with strakes. They focused on vortex-induced vibration of a bare cylinder and one fitted with strakes. They also suggest, through observation of iso-surfaces and streamlines, that the mechanisms for VIV suppression are the ones cited above: the lack spanwise correlation and the vortices formation farther downstream.

Bearing in mind the applications of strakes as VIV suppressors and the not yet well established physical mechanism of its effectiveness, we tackle this problem in its simplest proposition: a fixed circular cylinder fitted with strakes. We intend to show, using numerical simulations around a fixed straked circular cylinder, that we can indeed attribute the main mechanism of VIV suppression to the decrease of spanwise correlation. By spanwise correlation, we mean a measure of similarity between span positions (see eq. (9)). The strakes' geometry governs the flow separation points along each spanwise position which gives rise to a smaller correlation along span. In order to compare the simulations results to particle image velocimetry (PIV) data, we evaluate the spanwise variation of the flow based on mean velocity fields. We introduce a velocity field spatial correlation (see subsection 2.4) to quantify the spanwise variation.

We also observe that the vortex wake is formed farther downstream and we can identify this as a secondary mechanism of VIV suppression. The above features of the flow are compared to experimental measurements with PIV technique. Still for the sake of completeness, we also present the resulting fluid forces on the body in comparison to experimental measurements.

2. METHODOLOGY

The strakes geometry is described in the following subsection. The numerical method and the simulations parameters are presented in another subsection. In the last subsection we propose the correlation of the flow fields in order to quantify

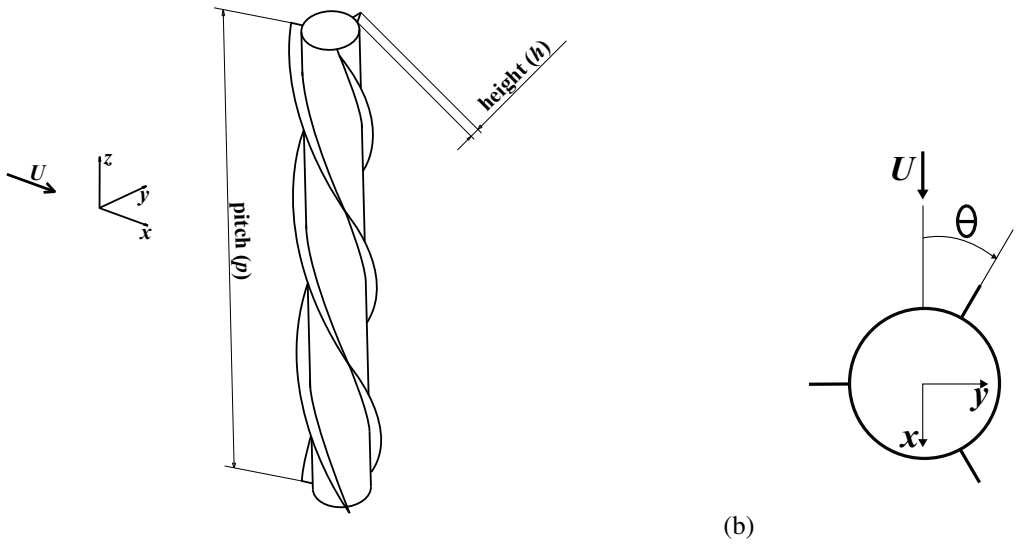

(a) (b)

Figure 1. Three-start helical strakes geometrical parameters. (a) Height and pitch definitions; (b) Angle of incidence definition.

the spanwise correlation.

2.1 Strakes

The helical strakes are defined by their height h and their pitch p as depicted in Fig. 1(a). In this paper, we use a common configuration of the helical strakes which is the three-start: this means that at each section there are three strakes equally space around the cylinder. Another geometrical definition we use herein is the angle of incidence θ of the far field velocity with respect to the cylinder section. It is defined as in Fig. 1(b).

Based on Korkischko and Meneghini (2010), we have chosen the helical strakes parameters to assure the suppression of the vortex-induced vibration so as to be reasonable a simulation of a fixed cylinder. The helical strakes parameters are presented in Tab. 1 with respect to the circular cylinder diameter d.

Table 1. Parameters of three-start helical strakes used in the simulations.

height	$0.20d$
pitch	$10d$

2.2 Numerical method

2.2.1 Lattice Boltzmann method

The numerical simulations are performed using Exa PowerFLOW software. This simulation code is based on the Lattice Boltzmann method for simulating fluid flow.

Let us introduce the lattice Boltzmann equation with the following form:

$$f_i\left(\vec{x}+\vec{c}_i\Delta t, t+\Delta t\right) - f_i\left(\vec{x},t\right) = C_i\left(\vec{x},t\right), \tag{1}$$

where f_i is the particle distribution function moving in the ith direction, according to a finite set of the discrete velocity vectors $\{\vec{c}_i : i = 0,\ldots,b\}$, while $\vec{c}_i\Delta t$ and Δt are space and time increments respectively. The collision term on the right hand side of Eq. 1 is employed in the most popular form known as the Bhatnagar-Gross-Krook (BGK) form (Qian *et al.*, 1992):

$$C_i\left(\vec{x},t\right) = -\frac{1}{\tau}\left[f_i\left(\vec{x},t\right) - f_i^{eq}\left(\vec{x},t\right)\right], \tag{2}$$

where τ is the single relaxation parameter, and f_i^{eq} is the local equilibrium distribution function dependent on local hydrodynamics properties (see Eq. 4). The basic hydrodynamic quantities, such as fluid density ρ and velocity $\vec{u}$ are the

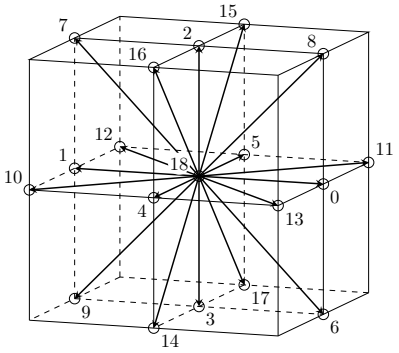

Figure 2. Three-dimensional D3Q19 lattice model. Numbers represent the discrete velocity directions of the model.

moment summations of the particle distribution functions:

$$\rho\left(\vec{x},t\right)=\sum_{i}f_{i}\left(\vec{x},t\right),\qquad\rho\vec{u}\left(\vec{x},t\right)=\sum_{i}\vec{c_{i}}f_{i}\left(\vec{x},t\right). \tag{3}$$

The lattice model used in the present simulations is the three-dimensional D3Q19 model (Qian *et al.*, 1992) depicted in Fig. 2. It represents the discrete possible velocity directions. For the D3Q19 model, the equilibrium distribution functions are of the form in Eq. 4 in order to the macroscopic hydrodynamics satisfy the conservations laws and the leading order recovered macroscopic equations are Galilean invariant at low Mach number. They are defined by the following equation

$$f_{i}^{eq}=\rho w_{i}\left[1+\frac{\vec{c}_{i}\vec{u}}{T}+\frac{\left(\vec{c}_{i}\vec{u}\right)^{2}}{2T^{2}}-\frac{\vec{u}^{2}}{2T}+\frac{\left(\vec{c}_{i}\vec{u}\right)^{3}}{6T^{3}}-\frac{\vec{c}_{i}\vec{u}}{2T^{2}}\vec{u}^{2}\right], \tag{4}$$

where the weighting parameters w_i are:

$$w_{i}=\begin{cases}1/18, & \text{for } i=0,\ldots,5 \text{ (axis-aligned directions)}\\ 1/36, & \text{for } i=6,\ldots,17 \text{ (bi-diagonal directions)}\\ 1/3, & \text{for } i=18 \text{ (rest particles)}\end{cases} \tag{5}$$

where T is the lattice temperature (in lattice units) which is set generally to $1/3$ for isothermal simulations.

Through Chapman-Enskog expansion (Chen *et al.*, 1992), one can recover the Navier-Stokes equations. The kinematic viscosity of the fluid is related to the relaxation time parameter τ by the relation:

$$\nu=\left(\tau-1/2\right)T. \tag{6}$$

The above equations form the Lattice Boltzmann Method (LBM) scheme for fluid dynamics used in the present work. Readers interested on more diverse details of the Lattice Boltzmann method should refer to Succi (2001).

2.2.2 Turbulence model

Due to the great difference of scales in turbulent flow, a model for the turbulent fluctuations is needed. Chen *et al.* (2003) proposes a lattice Boltzmann equation extension with turbulence model by replacing its molecular relaxation time scale τ with an effective turbulent relaxation time scale τ_{eff}, where τ_{eff} can be derived from a systematic renormalization group (RG) procedure. Chen *et al.* (2003) derived the following relation for the effective turbulent relaxation time scale relation:

$$\tau_{\text{eff}}=\tau+C_{\alpha}\frac{k^{2}/\varepsilon}{T(1+\tilde{\eta}^{2})^{1/2}} \tag{7}$$

where $\tilde{\eta}$ is a combination of a local strain parameter ($\eta=k|S|/\varepsilon$), local vorticity parameter ($\eta_{\omega}=k|\Omega|/\varepsilon$) and helicity parameters.

A modified k-ε two-equation model based on the original RG formulation describes the subgrid turbulence contributions (Yakhot and Orszag, 1986) and it is given by

$$\begin{aligned}\rho\frac{Dk}{Dt}&=\frac{\partial}{\partial x_{j}}\left[\left(\frac{\rho\nu_{0}}{\sigma_{k_{0}}}+\frac{\rho\nu_{T}}{\sigma_{k_{T}}}\right)\frac{\partial k}{\partial x_{j}}\right]+\tau_{ij}S_{ij}-\rho\varepsilon\\ \rho\frac{D\varepsilon}{Dt}&=\frac{\partial}{\partial x_{j}}\left[\left(\frac{\rho\nu_{0}}{\sigma_{\varepsilon_{0}}}+\frac{\rho\nu_{T}}{\sigma_{\varepsilon_{T}}}\right)\frac{\partial\varepsilon}{\partial x_{j}}\right]+C_{\varepsilon_{1}}\frac{\varepsilon}{k}\tau_{ij}S_{ij}-\left[C_{\varepsilon_{2}}+C_{\alpha}\frac{\tilde{\eta}^{3}(1-\tilde{\eta}/\eta_{0})}{1+\beta\tilde{\eta}^{3}}\right]\rho\frac{\varepsilon^{2}}{k}\end{aligned} \tag{8}$$

The parameter $\nu_T = C_\alpha k^2/\varepsilon$ is the eddy viscosity in the RG formulation. All dimensionless coefficients are the same as in the original models in Yakhot and Orszag (1986). The above equations are solved on the same lattice using a modified Lax-Wendroff like explicit time marching finite difference scheme.

2.3 Simulation parameters

The computational simulation is of the incompressible flow with Reynolds number $\mathrm{Re} = 1{,}000$ based on the bare circular cylinder diameter using turbulence model. The Reynold number of choice is due to the experimental data available from the water channel experiments in NDF-EPUSP facility. One simulation with $\mathrm{Re} = 10{,}000$ was also performed but no significant differences were perceived in the flow field results presented herein.

The flow domain is $62.5d$ upstream, $187.5d$ downstream, $62.5d$ sideways and a spanwise periodic length one strake pitch $p = 10d$. This computational domain is larger than the usual found in the literature, see for instance Carmo *et al.* (2008). The boundary conditions are periodicity in the spanwise direction, inflow velocity U_∞ on the upstream and sideways boundaries, with turbulence level of 1% and outflow with constant pressure on the downstream boundary.

The grid resolution of the simulation is 128 cells per cylinder diameter near the body. This resolution was based on simulations of a bare cylinder with the same flow conditions cited above while testing different refinements: the simulated flow converged to a drag coefficient of $C_D \simeq 1.15$. Further refinement did not change significantly the drag coefficient. Still, the simulated drag coefficient of the bare cylinder is higher than the experimental value ~ 1.04 (see Fig. 6). This can be attributed to the turbulent boundary layer model. Nevertheless, the flow around a cylinder fitted with strakes is mainly governed by the strakes' sharp edges, as later shown herein, and seemly the boundary layer plays a slightly lesser significant role. To further support the resolution of choice, Brès *et al.* (2010) have simulated the flow around two cylinders in tandem arrangement with $\mathrm{Re} = 1.66 \times 10^5$ and employed the same grid resolution of 128 cells per diameter.

The time step of the simulation using Lattice Boltzmann method is tied to the grid resolution and the lattice temperature. For the simulations herein, the non-dimensional time step is $\Delta t U_\infty/d = 6.63 \times 10^{-4}$.

The simulation parameters are summarized in Tab. 2.

Table 2. Summary of simulation parameters.

Incompressible flow with turbulence model	
Reynolds number	$1{,}000$
Domain size	
	$62.5d$ upstream and $187.5d$ downstream
	$62.5d$ sideways and $10d$ spanwise
Boundary conditions	
	inflow upstream and sides
	outflow downstream and periodic span
Grid resolution	128 cells per diameter
Non-dimensional time step	6.63×10^{-4}

2.4 Flow field correlation

In order to verify whether the geometrical periodicity presented by the three-start configuration of the helical strakes generates a wake flow with the same spanwise periodicity, a correlation criterion between the different spanwise planes is proposed (Korkischko and Meneghini, 2011).

This spatial correlation is based on the mean velocity field planes orthogonal to the cylinder axis. As we are interested in the near wake region and the PIV area of measurement is small, we restrict our plane of evaluation to the near wake.

The correlation $\mathcal{C}_j$, with respect to a reference plane j in $z = z_j$, is calculated using Eq. (9).

$$\mathcal{C}_{ij} = \sum_{i=0}^{N-1} \frac{\mathbf{V}|_{z=z_j}}{\|\mathbf{V}|_{z=z_j}\|} \cdot \frac{\mathbf{V}|_{z=z_i}}{\|\mathbf{V}|_{z=z_i}\|} \tag{9}$$

where j denotes the reference plane, i is run through the N planes used in the evaluation, $\mathbf{V}_{z=z_i}$ is the vector of velocity magnitudes in the plane $z = z_i$, and $\|\ \|$ means the Euclidean vector norm.

We calculate the correlation using the N planes as the reference plane. Afterwards, we take the average correlation for a given space interval. The resulting coefficient $\mathcal{C}$ is a function of spanwise spacing Δz, which can be seen in terms of angle of incidence θ.

3. RESULTS

The computational simulations of the flow around a cylinder fitted with strakes were realized with geometrical parameters of the strakes in Tab. 1 and parameters in Tab. 2. We simulated 100 vortex shedding cycles of a bare cylinder at this Reynolds number $1{,}000$.

Figure 3(a) presents a snapshot of the flow by the end of the simulation. The planes are colored by vorticity in z direction and they represent different angles of free flow incidence. First, we observe in Fig. 3 that there is not a clear vortex wake, indicating that the strakes cause the vortices to be formed farther downstream. This is ratified by the iso-surfaces in Fig. 3(b). Another feature in Fig. 3(a) is that the slices of the flow differ considerably suggesting that they are not correlated or in phase. Figure 3(b) also shows the lack of correlation and it highlights the spanwise periodicity of the flow induced by the strakes geometry. As a consequence of both features cited above, we expect low oscillations of the lift coefficient (Fig. 6), which is discussed by the end of this section.

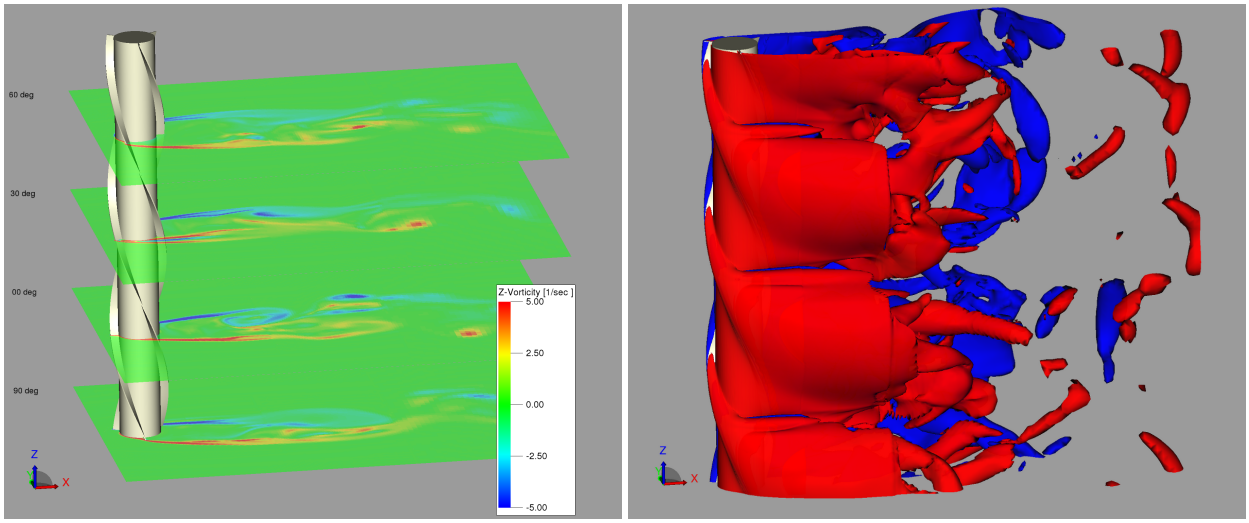

(a) (b)

Figure 3. Instantaneous snapshots from the computational simulation of the flow. (a) z-vorticity contour on slices, from blue $\omega_z = -5\text{s}^{-1}$ to red $\omega_z = 5\text{s}^{-1}$; (b) Iso-surfaces of z-vorticity, $\omega_z = -2\text{s}^{-1}$ in blue and $\omega_z = 2\text{s}^{-1}$ in red.

Before we discuss the correlation evaluation to the mean field, we analyze some features that can be observed in the mean fields. The aspects highlighted on the discussion of the instantaneous flow field from Fig. 3 have similar counterparts in the mean flow fields.

The main feature observed in each Fig. 4(a)-(d), is that the shear layers are distant from each other. This affects the interaction between them, consequently the vortices are formed farther downstream. A direct consequence is the smaller amplitude of lift on each section.

If we consider the variation of the mean flow along the spanwise direction, we note from Fig. 4 that we may expect a decrease in correlation due to the geometry of the section. The different tendencies of the mean flow on each section contributes to lower the lift coefficient of the whole body.

From the analysis of the mean fields we list the two main mechanisms of the strakes effectiveness: the strakes geometry contributes to a decrease of the spanwise correlation of the flow, and the strakes increase the distance between the two separated shear layers making the formation of vortices to occur farther downstream.

Figure 4 depicts the mean flow fields of four spanwise positions. We can note that the strakes govern the flow separation points along each spanwise position. The fields depend essentially on the angle of incidence of the free flow on that cylinder section. We propose to quantify the difference of each section by applying he correlation coefficient presented in Eq. (9).

As mentioned in the methodology section, we are interested in the near wake region since it presents the greatest differences of velocity and it is the region of action of most VIV suppressors. We employ the velocity magnitude in the plane to compute the correlation coefficient.

The region considered in the correlation of the experimental data is the plane of the PIV measurement. Table 3 compiles the information of the PIV plane and the plane considered in the evaluation of the correlation from computational simulation data is in Tab. 4. The PIV plane considers a region in the transverse direction that is wider than the simulation data plane.

The computed correlation coefficient is presented in Fig. 5. The correlation has a peak every $120°$, which means every $1/3$ of the strakes pitch. This is associated to the strake configuration of choice, a three-start configuration for the helical

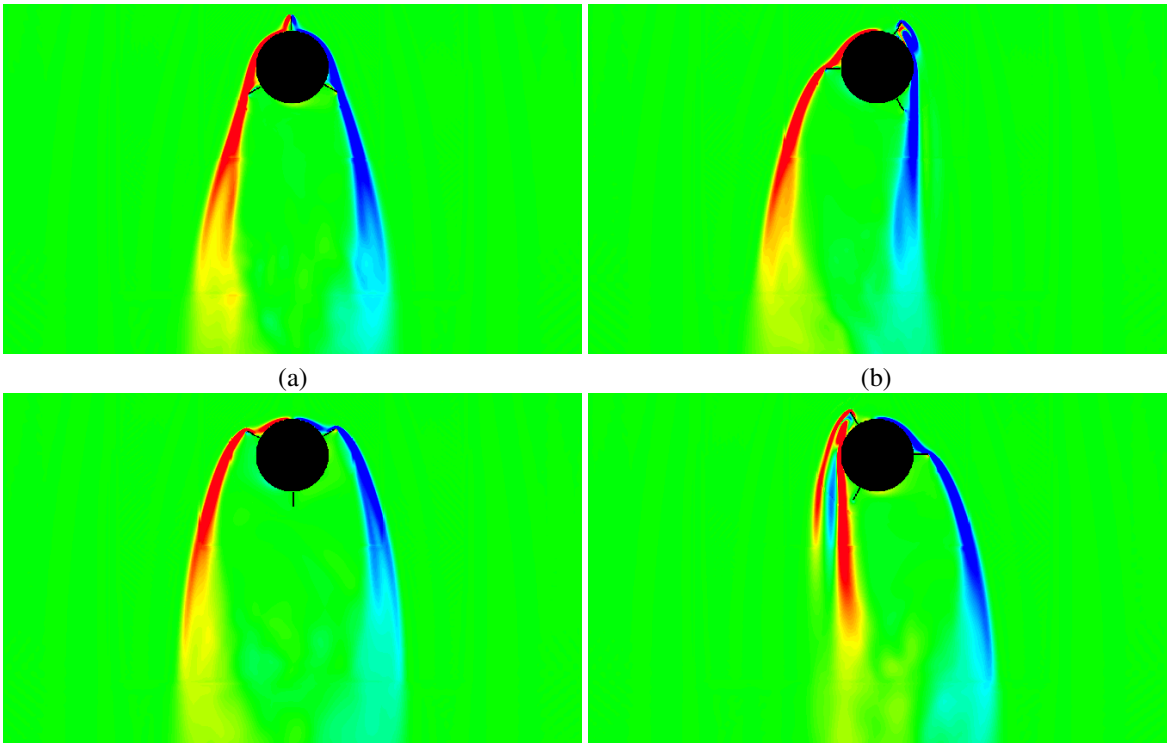

Figure 4. z-vorticity contour of the mean flow of the computational simulation. (a) $\theta = 0°$; (b) $\theta = 30°$; (c) $\theta = 60°$; (d) $\theta = 90°$.

Table 3. PIV plane of measurement considered in the correlation evaluation.

Cylinder center	$x = 0.0d$ and $y = 0.0d$
Streamwise position x	$0.50d$ to $5.25d$
Transverse position y	$-3.35d$ to $3.50d$

strakes: the cylinder section is the same every $1/3$ of the pitch. Hence, it is reasonable to consider that the mean flow has a $1/3$-pitch spanwise periodic length from the correlation in Fig. 5. We conclude that the geometrical periodicity governs the mean flow periodicity.

Still, we highlight the difference between the experimental data correlation and the simulation data correlation in Fig. 5. We attribute this difference to two causes: primarily, the planes of measurement are different, the greater far field region is considered, the smaller is the decrease of correlation in the spanwise direction; secondarily, there is a difference in the measurement resolution, the simulated data is much finer than from PIV measurements.

Finally, we compute the fluid force coefficients to compare with experimental data. Figure 6 shows the resulting instantaneous lift coefficient (dashed red line) and instantaneous drag coefficient (solid blue line) for the flow around a circular cylinder fitted with three-start helical strakes with $p = 10d$ and $h = 0.2d$. The time axis was normalized with the Strouhal frequency from a bare circular cylinder with $\mathrm{Re} = 1{,}000$. The mean drag coefficient measured in the experimental run of the cylinder fitted with strakes is shown in Fig. 6 as a dot-dashed line. We present the bare cylinder drag coefficient with a dotted line as reference value with $\mathrm{Re} = 1{,}000$. Table 5 summarizes the values cited above and it also shows the RMS value of C_L measured from the experimentof with the cylinder fitted with strakes in the water channel in comparison to the simulated value.

As expected, the drag coefficient of a cylinder with strakes is higher than the coefficient of a bare cylinder if the cylinder is not oscillating. We can observe in Fig. 6 that the drag coefficient from the computational simulation is slightly higher than the experimental measurements. Table 5 presents the values. The mean drag from computational simulation is around 2% higher than the experimental measure.

In Fig. 6, the instantaneous lift coefficient from the simulation has oscillations around zero value with very small amplitudes. This corroborates the lack of correlation along the spanwise direction introduced by the strakes. This amplitude of lift coefficient can hardly induce vibration.

Table 4. Simulation plane of measurement considered in the correlation evaluation.

Cylinder center	$x = 0.0d$ and $y = 0.0d$
Streamwise position x	$0.70d$ to $6.00d$
Transverse position y	$-1.50d$ to $1.50d$

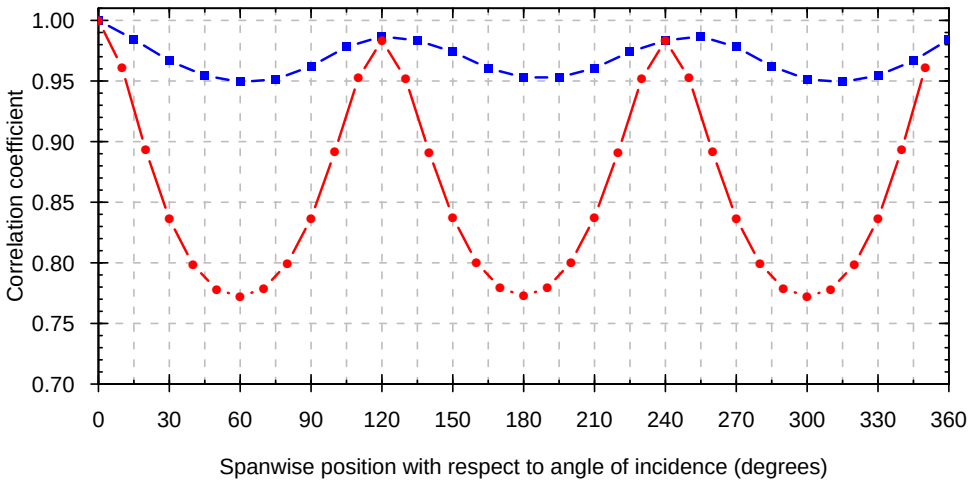

Figure 5. Correlation coefficient $\mathcal{C}$ from Eq. 9. Red circles line: current computational simulation; Blue squares line: experimental from PIV in Korkischko and Meneghini (2011).

4. CONCLUSIONS

In this brief paper, we infer the mechanism of suppression of vortex-induced vibration by using helical strakes. There are two mechanisms of suppression highlighted herein: the main one is the decrease in the vortex shedding correlation along the span, whilst a secondary one is the vortex wake formation farther downstream. Each of them affects differently the dynamics of the flow: the former breaks the correlation of the forces along the spanwise direction resulting in a low net lift force on the body, while the latter diminishes the amplitude of sectional lift.

The support of the aforementioned allegations is presented. First, the near wake of the cylinder fitted with strakes in Fig. 3 is not as well defined as that observed downstream a bare cylinder. This can also be inferred from the mean flow fields. The mean field shear layers are distant from each other, resulting in a weaker interaction between them, hence a vortex formation farther downstream. This is associated to the secondary mechanism of suppression.

The primary mechanism of suppression is corroborate by the flow field visualization and the spanwise field correlation proposed. Considering the instantaneous iso-vorticity surfaces in Fig. 3 and the mean vorticity field of the slices in Fig. 4, we may infer that the different cross-sections of the body along the spanwise direction governs the spanwise behavior of the fluid flow. As a consequence, we observe a very low net lift coefficient in Fig. 6 and a spanwise periodicity of the iso-vorticity surfaces and mean field slices.

The mean flow spanwise periodicity is further supported by the correlation proposed in Eq. 9. Both simulation and PIV data demonstrate similar tendency: they present a $1/3$-pitch spanwise periodic length due to the geometry of the three-start helical configuration of the strake. Still we highlight that the differences between the simulation and the experiments correlation curves can be explained by the distinct sizes of the planes of measurement, and by a difference in the spatial sampling resolution.

All in all, the remarks based on the simulation herein suggest that both the lack of flow correlation along the spanwise direction and the wake formation farther downstream compose the mechanism of suppression of vortex-induced vibration of the helical strakes, the former being the main mechanism.

5. ACKNOWLEDGEMENTS

The authors are grateful to FINEP-CTPetro, CNPq, and Petrobras for providing them a research grant for this project. R.S.G. and I.K. would also like to acknowledge FAPESP for the scholarship provided during the development of this work. All experimental and computational resources were provided by NDF-USP.

Table 5. Mean drag coefficient and RMS lift coefficient calculated from present simulation and experimental data for Reynolds number 1,000.

	Cylinder with strakes		Bare Cylinder
	Simulated	Experimental	Experimental
$C_{D_{\text{mean}}}$	1.33	1.3	1.04
$C_{L_{\text{RMS}}}$	0.025	0.03	0.06

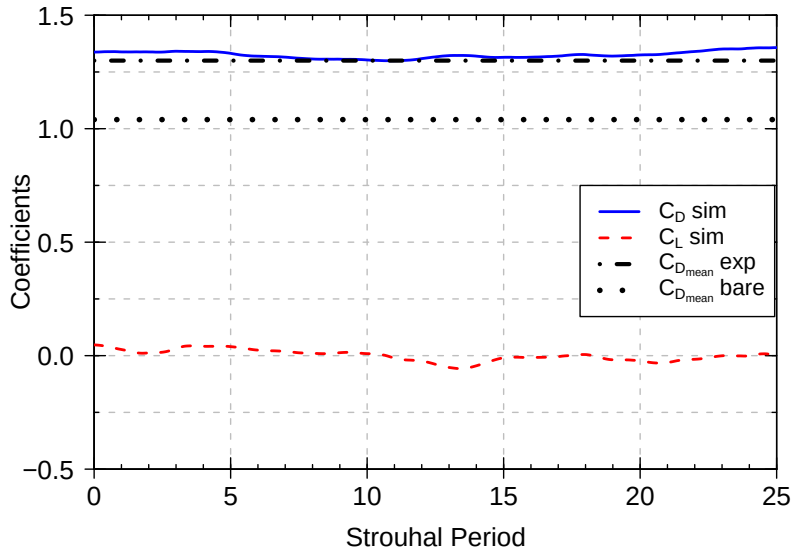

Figure 6. Force coefficients for a circular cylinder fitted with strakes from computational simulation. The Strouhal period refers to the Strouhal value of a bare circular cylinder. Solid blue line: current simulation instantaneous drag coefficient; Dashed red line: current simulation instantaneous lift coefficient; Horizontal dot-dashed line: experimental drag coefficient; Horizontal dotted line: experimental drag coefficient of a bare cylinder. Both experimental values are in Korkischko and Meneghini (2011).

6. REFERENCES

Bearman, P.W., 1984. "Vortex shedding from oscillating bluff bodies". *Annual Review of Fluid Mechanics*, Vol. 16, pp. 195–222.

Brès, G.A., Wessels, M. and Noelting, S., 2010. "Tandem cylinder noise predictions using Lattice Boltzmann and Ffowcs Williams-Hawkings methods". In *16th AIAA/CEAS Aeroacoustics Conference*. Paper number AIAA 2010-3791.

Carmo, B.S., Sherwin, S.J., Bearman, P.W. and Willden, R.H.J., 2008. "Wake transition in the flow around two circular cylinders in staggered arrangements". *Journal of Fluid Mechanics*, Vol. 597, pp. 1–29. doi: 10.1017/S0022112007009639.

Chen, H., Chen, S. and Matthaeus, W., 1992. "Recovery of the Navier-Stokes equations using a Lattice-gas Boltzmann method". *Physical Review A*, Vol. 45, pp. 5339–5342.

Chen, H., Kandasamy, S., Orszag, S., Shock, R., Succi, S., and Yakhot, V., 2003. "Extended Boltzmann kinetic equation for turbulent flows". *Science*, Vol. 301, pp. 633–636.

Choi, H., Jeon, W.P. and Kim, J., 2008. "Control of flow over a bluff body". *Annual Review of Fluid Mechanics*, Vol. 40, pp. 113–139.

Constantinides, Y. and Oakley, O.H., 2006. "Numerical prediction of bare and straked cylinder VIV". In W.L. Kuehnlein and D. Valentine, eds., *Proceedings of 25th International Conference on Offshore Mechanics and Arctic Engineering, OMAE*. Hamburg, Germany.

Korkischko, I. and Meneghini, J.R., 2010. "Experimental investigation of flow-induced vibration on isolated and tandem circular cylinders fitted with strakes". *Journal of Fluids and Structures*, Vol. 26, No. 4, pp. 611 – 625.

Korkischko, I. and Meneghini, J.R., 2011. "Volumetric reconstruction of the mean flow around circular cylinders fitted with strakes". doi:10.1007/s00348-011-1127-x. Accepted for publication in Experiments in Fluids.

Qian, Y., d'Humieres, D. and Lallemand, P., 1992. "Lattice BGK models for the Navier-Stokes equation". *Europhysics Letters*, Vol. 17, pp. 479–484.

Succi, S., 2001. *The Lattice Boltzmann Equations for Fluid Dynamics and Beyond*. Numerical Mathematics and Scientific Computation. Oxford University press.

Williamson, C.H.K. and Govardhan, R., 2004. "Vortex-induced vibrations". *Annual Review of Fluid Mechanics*, Vol. 36, pp. 413–455.

Yakhot, V. and Orszag, S.A., 1986. "Renormalization group analysis of turbulence. I. basic theory". *Journal of Scientific Computing*, Vol. 1, No. 2, pp. 3–51.

Zdravkovich, M.M., 1981. "Review and classification of various aerodynamic and hydrodynamic means for suppressing vortex shedding". *Journal of Wind Engineering and Industrial Aerodynamics*, Vol. 7, pp. 145–189.

7. Responsibility notice

The authors are the only responsible for the printed material included in this paper.